



THE UNIVERSITY *of* EDINBURGH

Edinburgh Research Explorer

Impact of windflow calculations on simulations of alpine snow accumulation, redistribution and ablation

Citation for published version:

Musselman, K, Pomeroy, J, Essery, R & Leroux, N 2015, 'Impact of windflow calculations on simulations of alpine snow accumulation, redistribution and ablation', *Hydrological Processes*, vol. 29, no. 18, pp. 3983–3999. <https://doi.org/10.1002/hyp.10595>

Digital Object Identifier (DOI):

[10.1002/hyp.10595](https://doi.org/10.1002/hyp.10595)

Link:

[Link to publication record in Edinburgh Research Explorer](#)

Document Version:

Peer reviewed version

Published In:

Hydrological Processes

General rights

Copyright for the publications made accessible via the Edinburgh Research Explorer is retained by the author(s) and / or other copyright owners and it is a condition of accessing these publications that users recognise and abide by the legal requirements associated with these rights.

Take down policy

The University of Edinburgh has made every reasonable effort to ensure that Edinburgh Research Explorer content complies with UK legislation. If you believe that the public display of this file breaches copyright please contact openaccess@ed.ac.uk providing details, and we will remove access to the work immediately and investigate your claim.



1 Impact of windflow calculations on simulations of
2 alpine snow accumulation, redistribution and ablation

3 K. N. Musselman^{1*}, J. W. Pomeroy¹, R. L. H. Essery², and N. Leroux¹

4 ¹Centre for Hydrology, University of Saskatchewan, Saskatoon, SK Canada

5 ²School of GeoSciences, University of Edinburgh, Edinburgh, UK

6 *Corresponding author; email: keith.musselman@usask.ca

7

8 **ABSTRACT**

9 Wind redistribution, radiation and turbulent heat fluxes determine seasonal snow accumulation
10 and melt patterns in alpine environments. Mathematical representations of windflow vary in
11 complexity and introduce uncertainty to snow modelling. To characterize this uncertainty, a
12 spatially distributed snow model that considers the physics of blowing snow transport and
13 sublimation and the energy fluxes contributing to snowpack ablation was evaluated for its ability
14 to simulate seasonal snow patterns around a windy alpine ridge in the Canadian Rockies. The
15 model was forced with output from three windflow models of varying computational complexity
16 and physical realism: i) a terrain-based empirical interpolation of station observations, ii) a
17 simple turbulence model, and iii) a computational fluid dynamics model. Compared to wind
18 measurements, the windflow simulations produced similar and relatively accurate (biases lower
19 than $\pm 1.1 \text{ m s}^{-1}$) wind speed estimates. However, the snow mass budget simulated by the snow
20 model was highly sensitive to the windflow simulation used. Compared to measurements,
21 distributed snow model depth and water equivalent errors were smallest using either of the two
22 turbulence models, with the best representation of downwind drifts by the computational fluid
23 dynamics model. Sublimation was an important mass loss from the ridge and windflow model
24 choice resulted in cumulative seasonal sublimation differences ranging from 10.5% to 19.0% of
25 seasonal snowfall. When aggregated to larger scales, differences in cumulative snowmelt and
26 snow transport were negligible but persistent differences in sublimation and snow-covered area
27 suggest that windflow model choice can have significant implications at multiple scales.
28 Uncertainty can be reduced by using physically based windflow models to drive distributed snow
29 models.

30

31 Keywords: blowing snow, wind, windflow model, alpine snow, sublimation

32 **1. INTRODUCTION**

33 The evolution of an alpine snowpack is greatly influenced by wind patterns. During and after
34 snowfall events, wind can redistribute snow from exposed areas and deposit it in sheltered
35 regions (Pomeroy *et al.*, 1997; Essery and Pomeroy, 2004). In the absence of vegetation,
36 topography and cumulative synoptic wind patterns determine the formation and persistence of
37 snow drifts in alpine environments (Greene *et al.*, 1999; Mott *et al.*, 2010; Schirmer *et al.*, 2011)
38 with important ecohydrological impacts (Williams and Melack, 1991; Brooks and Williams,
39 1999; Walker *et al.*, 2001; Wipf *et al.*, 2009). Particularly in mid-winter, turbulent energy
40 exchange at the snow surface can exceed radiation in importance and result in sublimation losses
41 (Marks and Dozier, 1992; Marks and Winstral, 2001). In cold, dry and windy environments, the
42 additional sublimation of blowing snow can be a substantial fraction of winter snowfall
43 (Pomeroy, 1989). During wind transport through an unsaturated atmosphere, snow particles are
44 well ventilated and undergo sublimation at rates exceeding that of the snow surface (Dyunin,
45 1959; Schmidt, 1972; Schmidt, 1986). Sublimation losses are important to consider in cold

46 regions hydrological models and estimation requires accurate windflow representation (Bowling
47 *et al.*, 2004).

48 Windflow also has important effects on snowmelt rates. Wind affects the spatial patterns
49 of meltwater availability indirectly through its influence on the end-of-winter snow distribution
50 (Pomeroy *et al.*, 1998; Pomeroy *et al.*, 2003; Grunewald *et al.*, 2010; Schirmer *et al.*, 2011; Egli
51 *et al.*, 2012) and directly through the turbulent exchange of temperature and water vapor between
52 the snow surface and the overlying air (Male and Granger, 1981). Pohl *et al.* (2006) and Menard
53 *et al.* (2014) have shown that variable wind exposure over complex terrain strongly influences
54 turbulent transfer to snow and subsequent melt rates.

55 In mountainous terrain, windflow patterns exhibit complex variability at spatial scales
56 that complicate efforts to map the influence of topography on wind speed and direction. Many
57 models rely on terrain-based empirical calibration on available measurements (e.g., Liston and
58 Sturm, 1998) or terrain shelter parameterizations based on assumed mean flow fields (e.g.,
59 Winstral and Marks, 2002). Linearized turbulence models such as the MS3DJH/3R model
60 (Walmsley *et al.*, 1982; Taylor *et al.*, 1983; Walmsley *et al.*, 1986) have been used to drive a
61 distributed blowing snow model (Essery *et al.*, 1999; Fang and Pomeroy, 2009). Linear
62 turbulence models represent windflow in a more physically realistic manner than the terrain-
63 based methods, but the simplified physics limits application to gentle slopes. More recently,
64 computationally intensive nonlinear turbulence models with stronger physical realism have been
65 used to downscale windflow patterns simulated by atmospheric models to simulate snow-drift
66 processes in complex terrain (Lehning *et al.*, 2008; Mott *et al.*, 2008; Bernhardt *et al.*, 2009;
67 Dadic *et al.*, 2010; Mott and Lehning, 2010). The approaches highlight a disparity in model
68 complexity in how windflow is commonly calculated in distributed snow model studies.

69 The objective of this paper is to explore warranted model complexity (Dornes *et al.*,
70 2008) for calculating seasonal snowpack evolution around an alpine ridge and to examine how
71 different windflow representations can propagate errors when used to drive a distributed blowing
72 snow and energy balance model. The study examines the impact of windflow calculations on
73 simulations of alpine snow redistribution, sublimation and subsequent melt; however, as in most
74 energy balance snow models, the turbulent advection from heterogeneous surface heating is not
75 considered. Specific research questions include: i) what is the relative accuracy of three
76 windflow models of varying computational complexity and physical realism? ii) how sensitive
77 are the snow mass balance calculations of a distributed blowing snow and energy balance model
78 to the representation of windflow? iii) do differences in snow dynamics calculated using
79 different windflow models persist as time and space scales increase?

80 **2. METHODS**

81 **2.1. Study site and measurements**

82 Fisera Ridge is an alpine study site in the Marmot Creek Research Basin (50°57'N; 115°12'W),
83 in the Canadian Rocky Mountains, Alberta, Canada (Figure 1). The site is located near treeline at
84 2320 m above sea level (asl) and the land cover is primarily bare soil and alpine grasses. The

85 ridge has an E-NE orientation and a generally perpendicular W-NW prevailing wind (Figure 2).
86 Any winter snow deposition on the windward (NW) slope is quickly wind-scoured and deposited
87 in a ~100 m zone on the leeward (SE) slope downwind of the ridge crest. The leeward and
88 windward slopes are $< 20^\circ$ and the ridge crest is rounded with a gradual change in slope (i.e.,
89 terrain curvature).

90 Three meteorological stations were located on the windward slope (windward station),
91 the top of the ridge (ridgetop station), and the leeward slope (leeward station) over a ~160 m
92 linear distance (Figure 1). The ridgetop station was located midway between the two stations and
93 slightly offset down the ridge crest (Figure 1). The ridgetop station recorded 15-minute averages
94 of 10-second measurements of air temperature and relative humidity (Campbell Scientific®
95 HMP45C212 probe with a Gill radiation shield at a height of 2.3 m), incoming shortwave and
96 longwave radiation (Kipp & Zonen® CNR1 net radiometer at a height of 1.4 m), snow depth
97 (Campbell Scientific® SR50-45 ultrasonic sensor), and wind speed and direction (R.M. Young®
98 05103AP at a height of 2.6 m). Snow depth (SR50-45) and wind speed were also recorded at the
99 windward and leeward stations with Met One® 013 three-cup anemometers at heights of 2.4 m
100 (windward) and 3.2 m (leeward). The nearest precipitation measurement was from a shielded
101 Geonor T200B gauge two km away in a forest clearing at 1845 m asl. After the study, an
102 identical gauge was installed in a sheltered area near the ridgetop station. The relationship
103 between precipitation values measured at the two locations for the 2009 water year was used to
104 estimate a multiplicative increase with elevation (1.86) to extrapolate measurements to the Fisera
105 Ridge study plot. Precipitation measurements were corrected for gauge under-catch as in
106 MacDonald *et al.* (2010). When air temperature was $\leq 0^\circ\text{C}$, relative humidity was estimated with
107 respect to ice following Yang *et al.*, (2010).

108 Thirteen manual snow surveys of depth and density were conducted between late-January
109 and May of 2008. Surveys consisted of two bisecting transects: a slope-parallel transect extended
110 from the windward station over the ridge and down beyond the leeward station and a shorter
111 ridge crest transect that extended below the ridgetop station (Figure 1). Snow depth was
112 measured every 1 - 3 m and snow density was measured every fifth depth measurement using an
113 ESC-30 snow tube and handheld spring scale when snow depth permitted ($\sim 20\text{ cm} < \text{depth} <$
114 $\sim 120\text{ cm}$). Otherwise, depth-integrated density measurements (1000 cm^3) were made at snowpits
115 near the automated stations. Snow density values from the nearest measurement location were
116 used to estimate SWE from survey depth measurements.

117 Airborne light detection and ranging (LiDAR) mapping was conducted in August, 2007
118 (snow-free) and again on 28 March, 2008 (snow-covered). A digital elevation model (DEM) and
119 a snow depth model at one-metre resolution were created from the data (Hopkinson *et al.*, 2012).
120 The aerodynamic surface roughness length estimated from LiDAR-derived vegetation height and
121 land surface classification is provided in Figure 1 (see Section 2.3.3). Note that the ridge and
122 immediate slopes are unvegetated to sparsely-vegetated.

123

124 **2.2. Snow model**

125 Meteorological observations from the ridgetop station were used to force a physically based
 126 snow redistribution, mass and energy balance model at 8 m grid spacing over a 1.024 km by
 127 1.024 km model domain centred on the Fisera Ridge study area (Figure 1). The average slope
 128 within the domain was $22^\circ \pm 7^\circ$ with a maximum slope value of 52° . The Distributed Snow
 129 Model (DSM) is a multi-layer soil and three-layer snow model that considers blowing snow and
 130 in-transit sublimation based on a simplified version (Essery et al., 1999) of the Prairie Blowing
 131 Snow Model (PBSM) (Pomeroy *et al.*, 1993; Pomeroy and Li, 2000). The snowpack compaction
 132 and thermodynamic routines are based on the JULES land surface model (Best *et al.*, 2011). The
 133 soil routine is described in Ménard et al. (2014). Meteorological observations other than wind
 134 speed and slope-projected shortwave radiation were assumed to be homogeneous. The windflow
 135 and blowing snow models were not fully coupled in that surface roughness (0.005 m) did not
 136 change with snow depth.

137 Wind speed variation due to topography was estimated with three different windflow
 138 models of varying computational complexity and physical realism (see Section 2.3). The
 139 windflow models produced maps of wind speed normalized by the ridgetop station values for
 140 eight wind directions. For each direction, normalized windflow maps were provided as a library
 141 to DSM to estimate wind speed over the domain from the measured wind speed and direction at
 142 the ridgetop station.

143

144 **2.3. Windflow models**

145 **2.3.1. ‘Liston-Sturm’ empirical windflow model**

146 The simplest of the three windflow models evaluated, an empirical model by Liston and Sturm
 147 (1998) (hereafter LS) was used with point wind speed and direction observed at the ridgetop
 148 station in conjunction with wind-topography relationships to extrapolate wind speed to grid cells.
 149 While the full LS model includes a diverting algorithm (Ryan, 1977) to estimate terrain-induced
 150 wind direction, the wind direction measured at the ridgetop station was uniformly applied to all
 151 grid cells for consistency with DSM assumptions. Terrain curvature, slope, and aspect were
 152 computed from the DEM following Liston and Sturm (1998). The average terrain curvature in
 153 four directions was computed with a 50 m length scale; estimated to be the average distance
 154 between the ridge crest and the middle of the two slopes, or approximately half the wavelength
 155 of Fisera Ridge. The upwind slope was computed for eight primary wind directions. For each
 156 grid cell (i,j) and wind direction (θ) a wind weighting factor, $W_{w_{i,j,\theta}}$, used to modify the
 157 measured wind speed, was estimated from the upwind slope ($\Omega_{s_{i,j,\theta}}$) and curvature ($\Omega_{c_{i,j}}$) terrain
 158 parameters, both scaled such that $-0.5 \leq \Omega_{s,c} \leq 0.5$, as in (Liston and Sturm, 1998):

$$159 \quad W_{w_{i,j,\theta}} = 1 + \gamma_s \Omega_{s_{i,j,\theta}} + \gamma_c \Omega_c \quad (1)$$

160 where the additional upwind slope and curvature weighting factors (γ_s and γ_c) with a range of
 161 $[0,1]$ were specified as 0.5 to equally weight the importance of the two terrain parameters in
 162 determining the local windflow around Fisera Ridge; this value is close to that determined

163 empirically in Liston and Elder (2006). The eight wind weight maps were provided as input to
164 DSM as described in Section 2.2.

165 **2.3.2. Mason-Sykes turbulence windflow model**

166 The second windflow model evaluated was a simple linear turbulence model developed from the
167 two-dimensional theoretical work of Jackson and Hunt (1975) by Walmsley *et al.* (1986) and
168 applied to three-dimensional (3-D) topography as in Mason and Sykes (1979) (hereafter, MS). It
169 solves linearized momentum equations using Fourier transforms of the topography. The model
170 offers more theoretical and physical realism than the empirical LS model, but does makes a
171 number of simplifying assumptions, including neutral stratification, and as a result it is only valid
172 over low hills (slopes < 25%). The MS model was run over the domain with a constant
173 roughness length of 0.005 m as in Essery *et al.* (1999). The model produced normalized wind
174 speed tables for the primary wind directions.

175

176 **2.3.3. Windsim® windflow model**

177 The third and most physically based windflow model examined was the commercial Windsim®
178 computational fluid dynamics (CFD) package (<http://windsim.com>) designed for the assessment
179 of wind energy resources in complex terrain. The CFD windflow model (hereafter WS), is based
180 on a 3-D Reynolds Averaged Navier Stokes (RANS) solver and uses a $k - \epsilon$ turbulence closure
181 scheme (Launder and Spalding, 1974). By solving the non-linear transport equations for mass,
182 momentum and energy, WS offers more theoretical and physical realism than the (linear) MS
183 turbulence model and may therefore be a more suitable windflow model in mountainous terrain.
184 A nesting technique was used to define the lateral boundary conditions of the (inner) 1.024 km x
185 1.024 km model domain. A 24 km x 24 km (outer) domain at 120 m horizontal resolution was
186 defined (Figure 1). The upper boundary conditions for both domains were specified with the
187 ‘constant pressure’ boundary option in WS, described to be most suitable for complex terrain.
188 The lateral boundary conditions of the outer domain were specified with a logarithmic velocity
189 profile < 500 m above the terrain; above this height a constant wind profile and 20 m s^{-1}
190 geostrophic wind speed was specified. The surface roughness of the outer domain was estimated
191 as a function of terrain elevation (Gravdahl and Vargvei, 1998). The logarithmic profile
192 assumption is only valid over flat terrain, which is violated here, but was only used to specify the
193 lateral boundary conditions of the outer domain to estimate the inner domain wind profile. The
194 nested domains were vertically discretized into 50 layers of 10 m thickness except for the lowest
195 layer, which was prescribed a 6 m thickness extending to 4 m above the DEM surface.
196 Experiments conducted with minimum heights < 4 m produced physically inconsistent values
197 indicative of numerical solution issues (not shown). Surface roughness lengths over the inner
198 domain (Figure 1) were estimated from vegetation height, h , derived from LiDAR
199 measurements. Roughness lengths for the inner WS simulations were specified as $0.5h$ for $h \geq 2$
200 m, $0.4h$ for $0.4 \leq h < 2.0$, and a minimum of 0.005 or $0.1h$ for $h < 0.4$ (Wallace and Hobbs,
201 2006). The specification of LiDAR-derived roughness lengths might be expected to improve

202 windflow performance over the two simpler models that either did not consider terrain roughness
203 (LS) or that considered the roughness length to be constant (MS).

204 The WS windflow model produced orthogonal u , v , w wind speed vector components for
205 each primary wind direction and specified height. Results from a height of 4 m above the inner
206 domain (snow-free) surface were used. For each wind direction, the horizontal wind speed was
207 calculated and the resulting wind field was normalized by the wind speed simulated at the pixel
208 corresponding to the location of the ridgetop station.

209 **2.4. Experimental design**

210 **2.4.1. Windflow model evaluation against measurements**

211 The three windflow models were evaluated for their relative skill at simulating the observed
212 wind speed on opposing slopes of the Fisera Ridge site. Windflow model accuracy was evaluated
213 against 15-minute data ($n=57,441$) for the October, 2008 to September, 2010 period when wind
214 data were available from all three stations. For each time step and windflow model, the ridgetop
215 station wind direction was used to reference the corresponding windflow map. The simulated
216 (normalized) wind speed values at locations of the windward and leeward stations were then
217 multiplied by the wind speed measured at the ridgetop station. The model root mean squared
218 error (RMSE) and bias values were computed. In addition, the modelled and measured wind
219 speed values were evaluated for time steps when the wind was out of the prevailing W-NW
220 direction, or roughly perpendicular to Fisera Ridge.

221 **2.4.2. Assessment of the impact of windflow calculation on simulated snowpack states**

222 Snow depth and SWE estimates from DSM forced by output from the three windflow models
223 were evaluated against multi-scale snowpack measurements. At the point-scale, simulated (daily)
224 snow depth values at the locations of the three stations were compared to automated
225 measurements. Modelled SWE was evaluated against field-based estimates derived from thirteen
226 (manual) snow density measurements and coincident (automated) snow depth measurements. At
227 the slope-scale, model simulations of SWE along the ‘T-shaped’ survey transect were evaluated
228 against survey measurements using nearest-neighbor averaging. Results for each windflow
229 model and for the respective transect-slope (i.e., windward, ridgetop, and leeward) are reported
230 in terms of the mean and standard deviation of the SWE error (‘modelled minus measured’). In
231 addition, spatially explicit snow depth simulations for 28 March, 2008 were qualitatively
232 compared to LiDAR-derived snow depth resampled from 1 m to 8 m grid spacing. Finally, the
233 impacts of the three windflow calculations on both the magnitude and timing of slope-averaged
234 simulated snow mass fluxes were evaluated. Simulated snow-covered area (SCA) and
235 cumulative seasonal snow transport, surface and blowing snow sublimation, and melt fluxes
236 were compared amongst the three windflow models. To evaluate whether different windflow
237 calculations impact the relative timing of simulated snow transport and sublimation, the
238 normalized and cumulative frequency of the hourly fluxes were binned into 12-hours periods
239 relative to the last precipitation event and the distributions were compared.

240 **3. Results**

241 The perpendicular orientation of Fisera Ridge to the prevailing wind direction (290°; Figure 2)
242 resulted in high measured wind speeds at the exposed windward and ridgetop station locations
243 with lower wind speeds on the sheltered leeward side. The average and standard deviation of the
244 15-minute wind speed measured at the windward, ridgetop, and leeward stations between 1
245 October, 2007 and 30 September, 2010 were $3.1 \pm 2.6 \text{ m s}^{-1}$, $2.3 \pm 2.2 \text{ m s}^{-1}$, and $2.3 \pm 1.5 \text{ m s}^{-1}$,
246 respectively. The pronounced wind speed variability over relatively short distances (~100 m) is
247 typical of windflow patterns in complex alpine terrain.

248 The three windflow models used to simulate wind speed on the opposing slopes produced
249 reasonable results compared to one year of measured wind speed (Figure 3). The RMSE and bias
250 values for all models were $< 1.7 \text{ m s}^{-1}$ and better than $\pm 1.1 \text{ m s}^{-1}$, respectively (Figure 4). Model
251 errors were generally similar as indexed by the correlation coefficients (Figure 3) and RMSE
252 values (Figure 4). The LS model slightly overestimated wind speed on both the leeward and
253 windward slopes (Figures 3 and 4). The MS model also underestimated wind speed on both
254 slopes and was the only model with negative wind speed biases (Figures 3 and 4). The WS
255 model exhibited near-zero mean model biases (Figure 4), but was prone to overestimating high
256 wind speeds (Figure 3).

257 Automated and manual snow measurements indicated that both the windward and ridgetop
258 sites were largely wind-scoured with seasonal average snow depths around 20 cm (Figure 5).
259 The deepest snowpack accumulated on the wind-exposed slopes during a series of spring
260 snowfall events when wet snow conditions restricted wind erosion (April - June). In contrast to
261 the wind-scoured slopes, a large drift accumulated on the leeward slope where snow depths
262 ranged between 100 and 180 cm and SWE exceeded 600 mm (Figure 5). At all sites, maximum
263 SWE occurred in early-May.

264 DSM forced by the three windflow models produced distinct differences in the seasonal
265 evolution, magnitude and location of simulated snow drifts (Figure 5). All DSM runs simulated
266 the mid-winter scour of the windward slope quite well, although the late-spring accumulation
267 events were uniformly overestimated. Compared to depth and SWE measurements at the
268 windward station, the MS turbulence model resulted in the lowest RMSE and bias values while
269 the empirical LS model, and particularly the CFD WS windflow model, caused overestimated
270 accumulation on the wind-exposed slope (see Table 1). At the ridgetop station, greater
271 differences in depth and SWE were simulated amongst the three model runs (Figure 5). As on
272 the windward slope, the MS-driven DSM best represented the frequent wind-scour of snow at the
273 ridgetop station with small depth and SWE biases of +3.5 cm and +11 mm, respectively (Table
274 1). Conversely, the LS-driven DSM erroneously simulated a large drift near the ridgetop station
275 with large depth and SWE biases of +73.9 cm and +419 mm, respectively (Figure 5 and Table
276 1). All DSM runs simulated drift formation on the leeward slope, but generally underestimated
277 the magnitude. The WS-driven DSM was closest to accurately simulating the leeward drift, with
278 depth and SWE biases of -10 cm and -66 mm, respectively (Figure 5 and Table 1). The MS- and
279 LS-driven DSM runs significantly underestimated the leeward SWE with mean biases of -157

280 mm and -259 mm, respectively. In general, improved SWE estimation was obtained with the
281 more physically based windflow models (MS and WS).

282 To better understand the cause of the simulated snowpack differences as determined at
283 the individual stations, the following metrics were evaluated along the 160 m linear transect
284 between the windward and leeward stations: 1) modelled wind speeds in the prevailing wind
285 direction (290°) relative to that measured at the ridgetop station (Figure 6a), 2) the change in the
286 modelled wind speed with distance du/dx (Figure 6b) and 3) the simulated SWE (Figure 6c)
287 over the ridge transect elevation profile (Figure 6d). The WS and LS models simulated a
288 decrease in wind speed from the windward to leeward sides while the MS model simulated wind
289 speeds on the ridgetop and windward slope, but a greater leeward decline in wind speed than the
290 other two models. Comparatively, the LS model simulated a relatively smooth wind speed
291 transition from the windward to leeward slopes. Breaks in the wind speed slope were greater in
292 the two turbulence models than the LS windflow model, but were simulated in different locations
293 along the ridge transect (Figure 6b). DSM modelled SWE (Figure 6c) varied significantly along
294 the ridge transect and that variability was windflow-model dependent. In general, DSM forced
295 by the two turbulence models simulated the greatest SWE on the leeward slope with DSM forced
296 by the WS model simulating the drift slightly closer to the ridgetop on the leeward side than the
297 MS-driven model. DSM forced by the empirical LS model erroneously simulated this drift
298 slightly to the windward side of the ridge.

299 Compared to the 28 March LiDAR snow depth estimates, the greatest differences in the
300 snow depth patterns from DSM forced by the three windflow models were amongst the empirical
301 LS model and the two turbulence models (Figure 7). The LS model resulted in a smoothly
302 varying snow-cover, deepest in proximity to the ridge crest and shallowest on both the windward
303 and leeward slopes. This is in contrast to the general understanding of snow accumulation around
304 alpine ridges (Pomeroy and Gray, 1995). By comparison, the two turbulence models resulted in
305 snow-cover patterns that were similar to the LiDAR derived snow cover with shallow snow and
306 snow-free areas on the windward and ridgetop zones, and deep and spatially heterogeneous drifts
307 covering much of the leeward slope. DSM forced by the two turbulence models simulated the
308 deepest snowpack (> 200 cm) in roughly similar locations, with the WS-driven DSM simulated
309 drift forming slightly closer to the ridge crest than the MS-driven model as described in the
310 transect evaluation. Note that the LiDAR product indicates deep drifts around small trees in the
311 southern- and eastern-most parts of the domain (see roughness heights in Figure 1); these areas
312 are included in the LiDAR depth map for completeness, but the inclusion of sparsely vegetated
313 areas prevents direct quantitative comparison of the measured and modelled products because the
314 DSM does not include vegetation roughness impacts on snowpack distribution and ablation.

315 Time-series of the seasonal evolution of simulated SWE is provided in Figure 8. Notably, the
316 29 April snow-cover extent is greater than the mid-winter distributions as a result of wetter
317 spring snow conditions and an associated lower likelihood of wind transport (Li and Pomeroy,
318 1997); this dynamic is recorded in the observations (Figure 5) and is generally captured by DSM
319 regardless of the windflow model.

320 Slope- and windflow model-specific SWE errors, computed as the seasonal average error
321 against data from the 13 snow surveys, show the general overestimation of SWE on the
322 windward slope and ridgetop by the LS-driven DSM (299 ± 135 mm and 311 ± 123 mm,
323 respectively) and, to a lesser extent, by the WS-driven DSM (138 ± 98 mm and 142 ± 91 mm,
324 respectively) (Figure 9). DSM forced by the MS turbulence model outperformed SWE estimated
325 by DSM forced by the other two windflow models at the two wind-exposed areas (35 ± 59 mm
326 and -23 ± 75 mm, respectively). On the leeward side of Fisera Ridge, DSM forced by any
327 windflow model underestimated SWE, but the WS model had significantly reduced errors ($-$
328 28 ± 91 mm) relative to DSM driven by the LS (-114 ± 97 mm) and MS (-131 ± 86 mm) windflow
329 models (Figure 9).

330 Differences in the impact of windflow calculations on snow regime estimation (i.e., depth
331 and SWE) were largely manifested in how the windflow models impacted the calculation of
332 seasonal snow fluxes including transport and sublimation. The greatest concurrence in simulated
333 transport, sublimation, melt, and SCA amongst the simulations forced by the three windflow
334 models occurred for the leeward slope (Figure 10), where wind speeds were lowest by all
335 estimates (Figure 2). The greatest deviation in cumulative blowing snow transport and
336 sublimation due to the windflow model occurred at the ridgetop station, where the MS-driven
337 DSM, found to be most accurate in terms of depth and SWE, generated the greatest snow
338 transport (out) and the highest sublimation fluxes. The WS- and LS-driven DSM simulated
339 $\sim 50\%$ and $\sim 25\%$, respectively, of the cumulative seasonal (total) sublimation losses calculated
340 by the MS-driven DSM. Only the LS model at the ridgetop station resulted in cumulative
341 transport estimates that differed in sign from the other models in that snow accumulated at the
342 ridgetop; the other model runs transported the snow off the ridgetop to the leeward slope.

343 The location of the greatest (total) sublimation losses was windflow model-dependent:
344 sublimation was highest on the windward slope with the LS- and WS-driven DSM, but on the
345 ridgetop with the MS-driven DSM (Figure 10). On average, cumulative surface sublimation
346 losses were approximately 50% of the cumulative blowing snow sublimation losses. Blowing
347 snow sublimation, reported as a percentage of cumulative seasonal snowfall, ranged from 8%
348 (leeward station) to 20% (windward and ridgetop stations). On average across the three slopes
349 (windward, ridgetop, and leeward rectangles in Figure 1), blowing snow sublimation losses with
350 the MS and WS models were 19% and 17.5% of cumulative seasonal snowfall, respectively,
351 while the average loss with the LS windflow model was only 10.5%. The sublimation source
352 also exhibited seasonality; blowing snow sublimation generally ceased at the beginning of
353 March, while most of the seasonal surface sublimation occurred from March through July
354 (Figure 10). Blowing snow sublimation estimated by DSM forced with the two turbulence
355 windflow models were similar to those in MacDonald et al. (2010) (19%) using the Cold
356 Regions Hydrological Model for the same year and at the same site but forced by measured
357 rather than simulated wind speeds.

358 To put the DSM results into context with those of model studies that treat blowing snow
359 sublimation as a self-limiting mechanism, the meteorological observations and DSM blowing

360 snow sublimation estimates from the largest blowing snow event of the 2008 winter are provided
361 (Figure 11). The event substantially redistributed alpine snow as is evident in the before and after
362 photographs. For simplicity, only results from DSM forced with the WS windflow model are
363 included in Figure 11. Following a period of light snow, low temperatures (-5° to -10°C), low
364 wind speeds (1 m/s), and saturated relative humidity with respect to ice (100%) on the morning
365 of Feb. 28, the snowfall stopped, air temperature plateaued at -4°C , relative humidity dropped to
366 $\sim 60\%$, and wind speed steadily increased (Figure 11). Two (hourly-average) wind speed maxima
367 were measured on Feb. 29: one at 01:00 (15 m/s) and the other at 07:00 (19.5 m/s). The DSM
368 simulated minor blowing snow fluxes (< 3.3 mm/hr; < 2 hrs.) corresponding to the timing of the
369 first wind speed maxima before a more substantial blowing snow event lasting ~ 4 hrs. with
370 maximum sublimation estimates of 13.3 mm/hr, 5.8 mm/hr, and 1.9 mm/hr on the windward,
371 ridgetop, and leeward sides, respectively occurring at 08:00 on Feb. 29 (Figure 11). Simulated
372 blowing snow sublimation stopped after four hours (10:00) and the wind speed dropped below
373 15 m/s. The air temperature measured at the ridgetop station steadily increased from -4.4°C at
374 the beginning of the large blowing snow event (05:00 Feb. 29) to -1.7°C (10:00) and the relative
375 humidity dropped slightly from 64% (05:00) to a minimum of 55% during the simulated blowing
376 snow maximum (08:00) and increased to 59% by the end of the event (10:00) (Figure 11).

377 Early in the melt period, cumulative snowmelt was insensitive to windflow representation,
378 and only became sensitive late in the season as differences in SCA depletion among the models
379 dictated meltwater availability (Figure 10). The leeward slope generally had the greatest SCA
380 with the latest snow-cover depletion, while the wind-scoured windward slope sustained an
381 intermittent snow-cover (Figure 10). The LS model resulted in the smoothest and most
382 homogeneous snow-cover (Figure 7) as well as the greatest SCA and latest snow-cover depletion
383 on all slopes. In contrast, the MS model resulted in the most variable SCA and the WS model
384 caused a gradual SCA change from intermittent (windward) to complete (leeward).

385 The results show that the windflow model choice can have significant implications for snow
386 regimes and snow fluxes at point- to slope-scales. When averaged over the full model domain the
387 differences in transport and melt were subtle to negligible; however, more appreciable
388 differences in sublimation and snow-cover depletion suggest that windflow model choice can
389 have important implications at multiple scales (Figure 10; right-most column). The windflow
390 model choice not only influenced the magnitude of seasonal blowing snow transport and
391 sublimation fluxes, but also the timing of these fluxes relative to snowfall events. In general,
392 DSM simulated a large majority of seasonal (hourly) blowing snow transport to occur between
393 13 and 24 hours after a snow event (Figure 12). On average, this trend was consistent across the
394 three slopes; however, depending on the windflow model, the fraction of seasonal blowing snow
395 transport during this 12 hour period varied by as much as 20%. Conversely, less than 1% of the
396 cumulative seasonal snow transport was simulated to occur more than 72-hours after a snowfall.
397 The windflow model choice had a lesser impact on the timing of sublimation losses. It is
398 interesting to note that $>90\%$ of the seasonal blowing snow sublimation losses and $<55\%$ of the

399 surface sublimation losses were simulated to occur within 36 hours of snowfall (Figure 12), with
400 the most surface sublimation occurring during the melt season (>72 hours).

401 **4. Discussion**

402 When forced with ridgetop windflow observations, all three windflow models adequately
403 captured the general pattern of high wind speeds on the exposed windward side of the alpine
404 ridge and lower wind speeds on the protected leeward side. The perpendicular nature of the
405 prevailing wind direction recorded at Fisera Ridge was remarkably persistent (Figure 2) as a
406 combined result of local terrain orientation and regional flow patterns. The slope-parallel
407 windflow persistence likely facilitated model accuracy by placing less emphasis on model skill at
408 simulating windflow direction relative to the reference station, and more emphasis on wind
409 velocity representation. As such, the model comparison represents a ‘best-case’ scenario that
410 provides important insight into the impacts of windflow calculations on simulations of alpine
411 snow redistribution and ablation.

412 Compared to measurements, the MS turbulence model had the greatest bias on both slopes
413 and highest RMSE on the windward slope (Figure 4). As previously noted, the empirical LS
414 windflow model weighting factors *upwind slope* and *curvature* were not determined from local
415 calibration, but specified as in previous empirical studies to be more consistent with how an
416 empirical windflow model might be applied to complex terrain. Despite the lack of local
417 calibration, when compared to measured wind speed on the two slopes the empirical LS model
418 performed as well as the WS model (in terms of the RMSE values) and better than the MS
419 model. For example, the MS simple turbulence model had the greatest average wind speed bias
420 of -0.95 m s^{-1} compared to the relatively smaller biases of the LS (0.25 m s^{-1}) and WS (0.05 m s^{-1})
421 windflow models (Figure 4). However, the windflow model evaluation against windward and
422 leeward slope wind speeds was a poor indicator of how wind speed errors might propagate into
423 DSM snow state errors and flux differences.

424 The three windflow models used to force DSM had appreciable and varying impact on the
425 calculation of seasonal snow mass balance (i.e., depth, SWE) and fluxes (i.e., transport,
426 sublimation and melt). The two turbulence models resulted in the deepest snowpack (> 200 cm)
427 in terrain-sheltered locations downwind of the ridgetop (Figures 7 and 8). By comparison, the
428 LS-driven DSM simulated a smoothly varying snow-cover, deepest in proximity to the ridgetop
429 and shallowest on both the windward and leeward slopes. The results suggest that improved
430 performance of the empirical LS windflow model might have been obtained from reducing the
431 distribution of weight on the curvature parameter and increasing the weight on the upwind slope
432 parameter; however, there is no guarantee that calibration of LS against wind speed alone would
433 have improved its performance in simulating the spatial distribution of SWE. The MS model
434 resulted in the lowest snowpack depth and SWE errors on the windward slope and ridgetop and
435 WS resulted in the lowest errors on the leeward slope (Figures 5 and 9; Table 1). These results
436 contrast with the evaluation of wind speed simulations discussed previously and imply that,

437 particularly in high-wind environments such as the ridgetop and windward slope where MS was
438 not the most accurate wind speed model, the representation of precisely how much the snow
439 transport wind speed threshold was exceeded may be of secondary importance for snow transport
440 calculations to the representation of wind speed spatial variability.

441 Modelled wind speed acceleration or deceleration indicated by positive and negative du/dx
442 values, respectively, (Figure 6b) determines whether snow simulated at a grid element is scoured
443 or deposited. The variation in the sign, magnitude, and spatial location of the simulated breaks in
444 wind speed among the three models indicate substantial fine-scale differences in windflow
445 representation (Figure 6b) that contribute to differences in the snow depth and SWE estimates
446 (Figure 6c). The smoothly varying snow-cover simulated by the LS-driven DSM is attributed to
447 the low variation and small (absolute) values of the du/dx values estimated by the LS windflow
448 model. By comparison, substantial variation in du/dx values simulated by the two turbulence
449 windflow models resulted in higher variability in simulated SWE (Figure 6c). The results suggest
450 that the turbulence models can represent windflow (and SWE) variability at two scales: i) slope-
451 scale terrain effects such as the windward and leeward sides of a ridge, and ii) small-scale (i.e., <
452 10 m) effects of slight terrain undulations. Differences in the exact position of wind speed breaks
453 over the ridge simulated by the turbulence models are likely due to structural disparities between
454 the linear (MS) and nonlinear (WS) windflow models. The empirical LS model may have been
455 able to capture these micro-scale wind speed variations with a smaller length-scale curvature
456 parameter, but such a parameter change may come at the expense of reduced slope-scale
457 accuracy, i.e., the curvature metric would then be more sensitive to small-scale terrain features
458 than slope-scale features such as the ridge. While overall errors in estimating snow depth and
459 SWE were generally smallest using either of the two turbulence windflow models compared to
460 the empirical model (Table 1), the ability of WS to estimate the leeward slope drift is notable for
461 two reasons: the snowpack mass balance at Fisera Ridge is dependent upon accurately simulating
462 upwind snow transport and in-transit sublimation; and the estimation of hydrologically important
463 leeward drifts is one of the main reasons to run a blowing snow model.

464 The models evaluated here assume that the wind direction is constant for all grid elements for
465 a given time step and do not consider terrain-induced alterations to the windflow direction. In
466 locations where the wind direction varies little and topography is simple, such as Fisera Ridge,
467 the computational efficiency of assuming a constant wind direction may outweigh potential
468 deficiencies in model performance due to the assumption. When wind direction over a domain is
469 unknown and terrain is more complex, then windflow patterns should be estimated based on
470 terrain characteristics (e.g., Ryan, 1977) or within a turbulence (e.g., Essery *et al.*, 1999) or
471 atmospheric (e.g., Mott *et al.*, 2014) model. Errors in the simulated drift formation compared to
472 measurements can accrue from the steady state assumption of the blowing snow model which
473 does not include a realistic temporal and spatial lag in the formation of snow deposition features
474 after a drop in wind speed on a lee slope. Non-steady-state blowing snow models are in their
475 infancy due to an incomplete understanding of turbulent snow particle interactions in complex

476 terrain. Despite these challenges, for the general application to areas of limited terrain
477 complexity such as presented here, the DSM results suggest that the more physically realistic
478 turbulence models are an example of warranted model complexity over the empirical LS
479 windflow model.

480 It is shown that cumulative seasonal snow transport and sublimation losses can be
481 significant and are sensitive to the windflow characterization. When averaged over the ridge, the
482 cumulative seasonal blowing snow sublimation losses relative to seasonal snowfall simulated by
483 DSM when forced with the MS (19%) and WS (17.5%) windflow models were similar to
484 estimates in MacDonald et al. (2010) (19%); note that the empirical LS windflow model caused
485 substantially lower estimates of blowing snow losses (10.5% of seasonal snowfall). The
486 differences imply that the windflow model choice can have significant implications on slope-
487 scale hydrology, ecology, and land surface representation; topics that require accurate
488 characterization of snow-cover duration and snow drift magnitude.

489 The largest blowing snow event of the 2008 winter was accompanied by increases in
490 both the 2.3 m air temperature and saturation deficit (Figure 11). The observations support
491 previous multi-height measurements made at a Canadian Prairie site (Pomeroy (1988) as
492 reported in Pomeroy and Li (2000)) where the process was attributed to dry air advection that
493 resulted from the mixing of initially stable boundary layers. The field examples suggest that
494 atmospheric boundary layer models must consider more thermodynamic phenomena than the
495 negative feedback process (Pomeroy and Li, 2000), particularly in wind-prone complex terrain
496 such as the Canadian Rocky Mountains. Future development of fully coupled atmospheric and
497 blowing snow models, validated by multi-height field observation, may provide useful insight
498 into the relative and often compensatory roles of blowing snow sublimation, moisture and
499 temperature feedback, and dry air advection mechanisms.

500 DSM estimated that the majority of cumulative seasonal snow transport and blowing snow
501 sublimation occurred in the 13 – 24 hour period after a storm event (Figure 12), illustrating the
502 importance of considering blowing snow threshold conditions and in-transit sublimation in
503 calculating snow redistribution. The results raise questions about how simple snow redistribution
504 models that immediately reallocate snowfall (e.g., Winstral and Marks, 2002) without
505 considering in-transit sublimation might result in the propagation of SCA and sublimation errors.
506 The accurate characterization of SCA is required to simulate the surface albedo, temperature, and
507 energy balance that are important for models that simulate atmospheric and hydrological
508 dynamics (Shook *et al.*, 1993; Pomeroy *et al.*, 1998). For example, the windflow model used to
509 force DSM impacted the simulation of late-lying snow patches known to enhance alpine albedo
510 and provide meltwater to alpine and subalpine lakes, wetlands and streams (Elder *et al.*, 1991).
511 During the spring and summer, water availability in alpine landscapes is influenced by winter
512 snow drift patterns, which in turn critically impacts vegetation distribution (Billings and Bliss,
513 1959; Walker *et al.*, 2001), soil moisture (Taylor and Seastedt, 1994), contaminant loading
514 (Pomeroy *et al.*, 1991) and nutrient cycling (Williams and Melack, 1991). At the slope-scale in

515 complex terrain, distributed blowing snow models require realistic windflow models to
516 accurately simulate these ecohydrological processes.

517 Finally, when DSM snow mass fluxes were spatially aggregated to include a larger area (~1
518 km²), which included less wind-prone areas, the windflow model-related differences in the time
519 evolution of aggregated snow transport and melt were subtle to negligible; however, there were
520 appreciable differences in sublimation and snow-cover depletion. The low sensitivity of
521 simulated spring melt fluxes to the windflow calculations may be underestimated but the error is
522 difficult to quantify due to the uncertainty in advection parameterisations for complex terrain
523 snowmelt calculations. While not considered here, turbulent advection of sensible heat can
524 influence snow-cover depletion rates (Shook *et al.*, 1993; Mott *et al.*, 2014). Turbulent advection
525 on Fisera Ridge is considered to be relatively small because while snow-cover is rapidly depleted
526 on the windward slope and ridgetop it persists in a large, continuous drift on the leeward slope
527 leading to one large snow patch with one leading edge. Thus, the spring snow-cover depletion
528 patterns at Fisera Ridge differ from the patchy snowpack with a wide distribution of snow patch
529 sizes and fetch lengths that have been studied in the Canadian Prairies or Arctic (Shook *et al.*,
530 1993; Granger *et al.*, 2002). The driving meteorological data for DSM was collected at a ridgetop
531 station that would be over snowcover when the entire domain was snow-covered and mostly
532 snow-free when only the leeward snowcover remained and so may have inherently
533 included some advected energy. While not explicitly considered, any additional turbulent energy
534 from advection may have propagated the reported differences in the estimated end-of-winter
535 SWE distribution amongst the windflow model-forced snow simulations due to inherent
536 feedback processes between SCA and the advection of sensible heat (Marsh and Pomeroy,
537 1996). Therefore, windflow model choice may have more influence on late-spring snow-cover
538 depletion rates and the time evolution of spatially aggregated spring snowmelt than reported
539 here.

540 The results suggest that the issue of warranted model complexity should be weighed in
541 careful consideration of the processes of interest, the model used, and the modelling objectives.
542 The variability of aggregated snow states, mass fluxes and SCA amongst windflow model-driven
543 DSM runs over landscape units corresponding to the windward, ridgetop and leeward slopes in
544 Figure 10 is substantial and suggests that improved simulations at the landscape unit scale can be
545 gained by using turbulence-based windflow models.

546 **5. Conclusions**

547 Compared to automated and manual measurements made on opposing sides of an alpine ridge,
548 DSM forced by the three windflow models produced distinct differences in the seasonal
549 evolution, magnitude and location of simulated snow drifts. The empirical LS-driven DSM
550 simulated a smoothly varying snow-cover, deepest in close proximity to the ridge crest and
551 shallowest on both the windward and leeward slopes. This was in contrast to the general
552 understanding of snow accumulation around alpine ridges. By comparison, the two turbulence
553 windflow model-driven DSM runs simulated snow-cover patterns that were similar to the

554 LiDAR-derived snow-cover with shallower snow and snow-free areas on the windward and
555 ridgetop zones, and a deeper drift covering much of the leeward slope. DSM forced by the two
556 turbulence models simulated the deepest snowpack (> 200 cm) in roughly similar locations. The
557 WS-driven DSM provided the most accurate snow simulation on the leeward slopes where large
558 drifts accumulate due to snow transport from upwind slopes. On average, cumulative surface
559 sublimation losses were approximately 50% of the cumulative blowing snow sublimation losses,
560 which were 19% and 17.5% of the cumulative seasonal snowfall with the MS and WS turbulence
561 models, but only 10.5% with the LS empirical windflow model. Strong seasonality was detected
562 in the sublimation source; blowing snow sublimation generally ceased at the beginning of March,
563 while most of the seasonal surface sublimation occurred from March through July. The location
564 of the greatest (total) sublimation losses was windflow model-dependent: sublimation was
565 highest on the windward slope with the LS- and WS-driven DSM, but on the ridgetop with the
566 MS-driven DSM. The results show that the windflow model choice can have significant
567 implications for calculating snow regimes and all snow mass fluxes at point- to slope-scales that
568 are important for alpine ecology and at landscape scales relevant to hydrological and climate
569 models that consider sub-grid or sub-basin variability.

570 **ACKNOWLEDGEMENTS**

571 Financial support was provided by NSERC, CRC, CERC, CFI, and AESRD. The authors thank
572 C. Hopkinson, Nakiska Mountain Resort, the University of Calgary Biogeoscience Institute,
573 Centre for Hydrology students and staff, and two anonymous reviewers..

574 **REFERENCES**

- 575 Bernhardt M, Zängl G, Liston G, Strasser U, Mauser W. 2009. Using wind fields from a high-resolution
576 atmospheric model for simulating snow dynamics in mountainous terrain. *Hydrological*
577 *processes*, **23**: 1064-1075.
- 578 Best M, Pryor M, Clark D, Rooney G, Essery R, Ménard C, Edwards J, Hendry M, Porson A, Gedney N.
579 2011. The Joint UK Land Environment Simulator (JULES), model description–Part 1: energy and
580 water fluxes. *Geoscientific Model Development*, **4**: 677-699.
- 581 Billings WD, Bliss L. 1959. An alpine snowbank environment and its effects on vegetation, plant
582 development, and productivity. *Ecology*: 388-397.
- 583 Bowling L, Pomeroy J, Lettenmaier D. 2004. Parameterization of blowing-snow sublimation in a
584 macroscale hydrology model. *Journal of Hydrometeorology*, **5**: 745-762.
- 585 Brooks PD, Williams MW. 1999. Snowpack controls on nitrogen cycling and export in seasonally snow-
586 covered catchments. *Hydrological Processes*, **13**: 2177-2190.
- 587 Dadic R, Mott R, Lehning M, Burlando P. 2010. Wind influence on snow depth distribution and
588 accumulation over glaciers. *Journal of Geophysical Research: Earth Surface (2003–2012)*, **115**.
- 589 Dornes PF, Pomeroy JW, Pietroniro A, Carey SK, Quinton WL. 2008. Influence of landscape aggregation
590 in modelling snow-cover ablation and snowmelt runoff in a sub-arctic mountainous
591 environment. *Hydrological Sciences Journal*, **53**: 725-740.
- 592 Dyunin AK. 1959. Fundamentals of the Theory of Snow Drifting. *Izvest. Sibirsk, Otdel. Akad. Nauk.*
593 *U.S.S.R.*, **12**: 11-24.

594 Egli L, Jonas T, Grünewald T, Schirmer M, Burlando P. 2012. Dynamics of snow ablation in a small Alpine
595 catchment observed by repeated terrestrial laser scans. *Hydrological Processes*, **26**: 1574-1585.

596 Elder K, Dozier J, Michaelsen J. 1991. Snow accumulation and distribution in an alpine watershed. *Water*
597 *Resources Research*, **27**: 1541-1552.

598 Essery R, Li L, Pomeroy J. 1999. A distributed model of blowing snow over complex terrain. *Hydrological*
599 *processes*, **13**: 2423-2438.

600 Essery R, Pomeroy J. 2004. Vegetation and topographic control of wind-blown snow distributions in
601 distributed and aggregated simulations for an Arctic tundra basin. *Journal of Hydrometeorology*,
602 **5**: 735-744.

603 Fang X, Pomeroy J. 2009. Modelling blowing snow redistribution to prairie wetlands. *Hydrological*
604 *processes*, **23**: 2557-2569.

605 Granger R, Pomeroy J, Parviainen J. 2002. Boundary-layer integration approach to advection of sensible
606 heat to a patchy snow cover. *Hydrological Processes*, **16**: 3559-3569.

607 Gravdahl AR, Vargvei N. 1998. Meso scale modeling with a reynolds averaged navier-stokes solver:
608 assessment of wind resources along the Norwegian coast. In: 31th IEA experts meeting. State of
609 the Art on Wind Resource Estimation.

610 Greene EM, Liston GE, Pielke Sr RA. 1999. Simulation of above treeline snowdrift formation using a
611 numerical snow-transport model. *Cold Regions Science and Technology*, **30**: 135-144.

612 Grunewald T, Schirmer M, Mott R, Lehning M. 2010. Spatial and temporal variability of snow depth and
613 ablation rates in a small mountain catchment. *Cryosphere*, **4**: 215-225.

614 Hopkinson C, Pomeroy J, Debeer C, Ellis C, Anderson A. 2012. Relationships between snowpack depth
615 and primary LiDAR point cloud derivatives in a mountainous environment. In: IAHS-AISH
616 publication, pp: 354-358.

617 Jackson P, Hunt J. 1975. Turbulent wind flow over a low hill. *Quarterly Journal of the Royal*
618 *Meteorological Society*, **101**: 929-955.

619 Launder BE, Spalding D. 1974. The numerical computation of turbulent flows. *Computer methods in*
620 *applied mechanics and engineering*, **3**: 269-289.

621 Lehning M, L[^]we H, Ryser M, Raderschall N. 2008. Inhomogeneous precipitation distribution and snow
622 transport in steep terrain. *Water Resour. Res.*, **44**: W07404. DOI: 10.1029/2007wr006545.

623 Li L, Pomeroy JW. 1997. Estimates of threshold wind speeds for snow transport using meteorological
624 data. *Journal of Applied Meteorology*, **36**: 205-213.

625 Liston GE, Elder K. 2006. A Meteorological Distribution System for High-Resolution Terrestrial Modeling
626 (MicroMet). *Journal of Hydrometeorology*, **7**: 217-234. DOI: 10.1175/jhm486.1.

627 Liston GE, Sturm M. 1998. A snow-transport model for complex terrain. *Journal of Glaciology*, **44**: 498-
628 516.

629 MacDonald M, Pomeroy J, Pietroniro A. 2010. On the importance of sublimation to an alpine snow mass
630 balance in the Canadian Rocky Mountains. *Hydrology and Earth System Sciences*, **14**: 1401-1415.

631 Male D, Granger R. 1981. Snow surface energy exchange. *Water Resources Research*, **17**: 609-627.

632 Marks D, Dozier J. 1992. Climate and energy exchange at the snow surface in the Alpine Region of the
633 Sierra Nevada: 2. Snow cover energy balance. *Water Resources Research*, **28**: 3043-3054.

634 Marks D, Winstral A. 2001. Comparison of snow deposition, the snow cover energy balance, and
635 snowmelt at two sites in a semiarid mountain basin. *Journal of Hydrometeorology*, **2**: 213-227.

636 Marsh P, Pomeroy J. 1996. Meltwater fluxes at an arctic forest-tundra site. *Hydrological Processes*, **10**:
637 1383-1400.

638 Mason P, Sykes R. 1979. Flow over an isolated hill of moderate slope. *Quarterly Journal of the Royal*
639 *Meteorological Society*, **105**: 383-395.

640 Mott R, Faure F, Lehning M, Lowe H, Hynek B, Michlmayr G, Prokop A, Schoner W. 2008. Simulation of
641 seasonal snow cover distribution for glacierized sites (Sonnblick, Austria) with the Alpine3D
642 model. *Annals of Glaciology*, **49**: 155-160.

643 Mott R, Lehning M. 2010. Meteorological Modeling of Very High-Resolution Wind Fields and Snow
644 Deposition for Mountains. *J Hydrometeorol*, **11**: 934-949. DOI: 10.1175/2010jhm1216.1.

645 Mott R, Lehning M, Daniels M, Lehning M. 2014. Atmospheric Flow Development and Associated
646 Changes in Turbulent Sensible Heat Flux over a Patchy Mountain Snow Cover. *Journal of*
647 *Hydrometeorology*.

648 Mott R, Schirmer M, Bavay M, Grünewald T, Lehning M. 2010. Understanding snow-transport processes
649 shaping the mountain snow-cover. *The Cryosphere*, **4**: 545-559.

650 Ménard C, Essery R, Pomeroy J. 2014. Modelled sensitivity of the snow regime to topography, shrub
651 fraction and shrub height. *Hydrology and Earth System Sciences Discussions*, **11**: 223-263.

652 Ménard CB, Essery R, Pomeroy J, Marsh P, Clark DB. 2014. A shrub bending model to calculate the
653 albedo of shrub-tundra. *Hydrological Processes*, **28**: 341-351.

654 Pohl S, Marsh P, Liston G. 2006. Spatial-temporal variability in turbulent fluxes during spring snowmelt.
655 *Arctic, Antarctic, and Alpine Research*, **38**: 136-146.

656 Pomeroy J. 1989. A process-based model of snow drifting. *Ann. Glaciol*, **13**: 237-240.

657 Pomeroy J, Davies T, Tranter M. 1991. The impact of blowing snow on snow chemistry. In: *Seasonal*
658 *Snowpacks*, Springer, pp: 71-113.

659 Pomeroy J, Gray D. 1995. Snowcover accumulation, relocation and management. *Bulletin of the*
660 *International Society of Soil Science* no, **88**.

661 Pomeroy J, Gray D, Landine P. 1993. The prairie blowing snow model: characteristics, validation,
662 operation. *Journal of Hydrology*, **144**: 165-192.

663 Pomeroy J, Li L. 2000. Prairie and Arctic areal snow cover mass balance using a blowing snow model.
664 *Journal of Geophysical Research: Atmospheres (1984–2012)*, **105**: 26619-26634.

665 Pomeroy J, Toth B, Granger R, Hedstrom N, Essery R. 2003. Variation in surface energetics during
666 snowmelt in a subarctic mountain catchment. *Journal of Hydrometeorology*, **4**: 702-719.

667 Pomeroy JW. 1988. Wind transport of snow. University of Saskatchewan, pp: 226.

668 Pomeroy JW, Gray DM, Shook KR, Toth B, Essery RLH, Pietroniro A, Hedstrom N. 1998. An evaluation of
669 snow accumulation and ablation processes for land surface modelling. *Hydrological Processes*,
670 **12**: 2339-2367. DOI: 10.1002/(sici)1099-1085(199812)12:15<2339::aid-hyp800>3.0.co;2-l.

671 Pomeroy JW, Marsh P, Gray DM. 1997. Application of a distributed blowing snow model to the Arctic.
672 *Hydrological Processes*, **11**: 1451-1464.

673 Ryan BC. 1977. A mathematical model for diagnosis and prediction of surface winds in mountainous
674 terrain. *Journal of Applied Meteorology*, **16**: 571-584.

675 Schirmer M, Wirz V, Clifton A, Lehning M. 2011. Persistence in intra-annual snow depth distribution: 1.
676 Measurements and topographic control. *Water Resources Research*, **47**.

677 Schmidt R. 1972. Sublimation of wind-transported snow--a model. USDA Forest Service research paper
678 RM-United States, Rocky Mountain Forest and Range Experiment Station.

679 Schmidt R. 1986. Transport rate of drifting snow and the mean wind speed profile. *Boundary-Layer*
680 *Meteorology*, **34**: 213-241.

681 Shook K, Gray D, Pomeroy J. 1993. Temporal variation in snowcover area during melt in prairie and
682 alpine environments. *Nordic Hydrology*, **24**: 183-183.

683 Taylor P, Walmsley J, Salmon J. 1983. A simple model of neutrally stratified boundary-layer flow over
684 real terrain incorporating wavenumber-dependent scaling. *Boundary-Layer Meteorology*, **26**:
685 169-189.

686 Taylor R, Seastedt T. 1994. Short-and long-term patterns of soil moisture in alpine tundra. *Arctic and*
687 *Alpine Research*: 14-20.

688 Walker D, Billings W, De Molenaar J. 2001. Snow–vegetation interactions in tundra environments. *Snow*
689 *ecology: an interdisciplinary examination of snow-covered ecosystems*: 266-324.

690 Wallace JM, Hobbs PV. 2006. *Atmospheric science: an introductory survey*. Academic press.

691 Walmsley J, Taylor P, Keith T. 1986. A simple model of neutrally stratified boundary-layer flow over
692 complex terrain with surface roughness modulations (MS3DJH/3R). *Boundary-Layer*
693 *Meteorology*, **36**: 157-186.

694 Walmsley JL, Salmon J, Taylor P. 1982. On the application of a model of boundary-layer flow over low
695 hills to real terrain. *Boundary-Layer Meteorology*, **23**: 17-46.

696 Williams MW, Melack JM. 1991. Solute chemistry of snowmelt and runoff in an alpine basin, Sierra
697 Nevada. *Water resources research*, **27**: 1575-1588.

698 Winstral A, Marks D. 2002. Simulating wind fields and snow redistribution using terrain-based
699 parameters to model snow accumulation and melt over a semi-arid mountain catchment.
700 *Hydrological Processes*, **16**: 3585-3603.

701 Wipf S, Stoeckli V, Bebi P. 2009. Winter climate change in alpine tundra: plant responses to changes in
702 snow depth and snowmelt timing. *Climatic Change*, **94**: 105-121.

703 Yang J, Yau M, Fang X, Pomeroy J. 2010. A triple-moment blowing snow-atmospheric model and its
704 application in computing the seasonal wintertime snow mass budget. *Hydrology and Earth*
705 *System Sciences*, **14**: 1063-1079.

706

707

708

709 Table 1. Snow depth and SWE errors for the snow simulations forced by the three windflow
710 models as evaluated against snow observations made at the three stations. The shaded cells
711 indicate the windflow model that produced the lowest error values for each station. Note that the
712 depth errors were calculated from mean daily automated measurements while the SWE errors
713 were the average error values computed on manual observations at near each station during 13
714 repeated snow surveys.

		RMSE			bias		
		windward	ridgetop	leeward	windward	ridgetop	leeward
Depth, cm	LS	22.1	83.4	53.7	16.6	73.9	-38.9
	MS	14.4	9.3	38.1	7.5	3.5	-22.7
	WS	29.3	25.7	27.0	21.4	20.9	-10.0
SWE, mm	LS	91	429	270	70	419	-259
	MS	57	38	170	37	11	-157
	WS	131	110	84	97	101	-66

715

716 FIGURE CAPTIONS

717 Figure 1: Study site map showing the nested model domains (24 km x 24 km with 150 m
718 elevation contour lines; 1.024 km x 1.024 km with 10 m elevation contour lines) centred on the
719 locations of three meteorological stations on the alpine Fisera Ridge in the Marmot Creek
720 Research Basin, Alberta, Canada (location indicated by the star in the upper-right panel). The
721 small maps at right (20 m elevation contour lines) indicate the (top): LiDAR-derived roughness
722 length values over the inner domain and (bottom): the locations of the snow survey transects
723 relative to the three meteorological stations. Rectangular domains used to compare spatially
724 averaged simulated fluxes representative of the windward, ridgetop, and leeward parts of Fisera
725 Ridge are shown.

726 Figure 2: Wind roses including the mean and maxima wind speeds for the windward, ridgetop
727 and leeward stations from 15-minute averaged data collected from October, 2008 to September,
728 2010 (n=57,441). Analysis was limited to time-steps when data were available from all three
729 stations. Note that wind direction was only measured at the ridgetop station and was assumed
730 representative of the two other stations for the purposes of the wind rose comparison.

731 Figure 3: Scatter plots of wind speed comparing modelled values (y-axes) from each of the three
732 windflow models (panel rows) to measured values (x-axes) at the windward (left panels) and
733 leeward (right panels) automated weather stations. The (linear) regression fits, coefficients of
734 determination (R^2), and correlation coefficients (r) are indicated.

735 Figure 4: Mean (bars) and standard deviation (lines) of modelled wind speed RMSE (top) and
736 bias (bottom) for the three windflow models compared to measurements at the windward and
737 leeward automated weather stations.

738 Figure 5: Measured snow depth (top) and SWE (bottom) compared to simulated values from the
739 three windflow models (lines) at the windward (left panel column), ridgetop (centre panel
740 column), and leeward (right panel column) stations.

741 Figure 6: Modelled a) seasonal mean wind speed normalized by the ridgetop station
742 observations, b) the change in mean wind speed with distance (du/dx), and c) snow water
743 equivalent (SWE) presented as the pixel-wise nearest-neighbor mean (lines) and standard
744 deviation (shading) near the time of seasonal maximum accumulation (May 1, 2008) along d) a
745 160 m linear (12 m vertical) transect from the windward to leeward sides of the alpine ridge.

746 Figure 7: The LiDAR-measured snow depth on Fisera Ridge on 28 March, 2008 (left) compared
747 to that simulated by DSM forced by wind speed output from the Liston-Sturm (LS), Mason-
748 Sykes (MS) and Windsim (WS) windflow models. The location of the windward (red marker),
749 ridgetop (black marker), and leeward (blue marker) stations are indicated. The elevation contour
750 lines are included.

751 Figure 8: Distributed maps of SWE (color scale) near the Fisera Ridge stations (markers) on the
752 dates of select snow surveys (panel rows) as simulated by DSM forced with output from the
753 three windflow models (panel columns). Elevation contour lines are included.

754 Figure 9: Model SWE error computed as the mean (bars) and standard deviation (lines) of
755 'modelled - measured' SWE averaged along the snow survey transects for 13 surveys on the
756 windward (left), ridgetop (centre), and leeward (right) sides of Fisera Ridge for the DSM model
757 forced by wind speed output from the Liston-Sturm (LS), Mason-Sykes (MS) and Windsim
758 (WS) windflow models.

759 Figure 10: Cumulative fluxes of snow transport, sublimation (total, surface and blowing snow
760 losses), melt, and snow covered area averaged within domains centered on the windward,
761 ridgetop, leeward, and the entire domain as simulated by DSM forced with wind speed output
762 from the Liston-Sturm (LS), Mason-Sykes (MS) and Windsim (WS) windflow models for the
763 2007-2008 snow season.

764 Figure 11: Measured values of wind speed, air temperature, precipitation (left axis) and relative
765 humidity (right axis) during a blowing snow event on February 29, 2008 at the Fisera Ridge
766 (ridgetop) station. Blowing snow sublimation rates estimated by DSM forced with windflow
767 output from the Windsim model at the locations of the windward, ridgetop and leeward stations
768 are included. Photographs from a field camera mounted on the ridgetop station looking northwest
769 toward the windward slope show snow cover before (15:00 Feb. 28) and after (12:00 Feb. 29) the
770 blowing snow event.

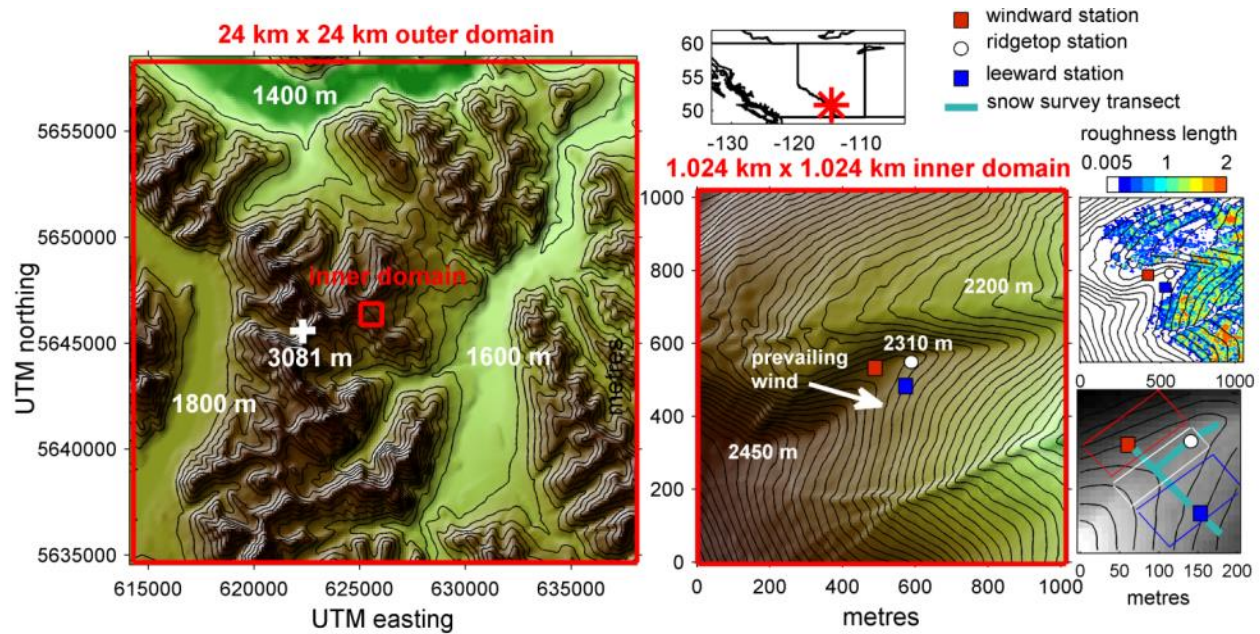
771 Figure 12: The timing of normalized (left y-axes) and cumulative (right y-axes) hourly seasonal
772 snow transport and sublimation (total, surface and blowing snow) fluxes, binned in 12-hour
773 intervals since the last snowfall (x-axes), as simulated by DSM forced by wind speed output
774 from the Liston-Sturm (LS), Mason-Sykes (MS) and Windsim (WS) windflow models for the
775 2007-2008 snow season.

776

777 Table 1. Snow depth and SWE errors for the snow simulations forced by the three windflow
 778 models as evaluated against snow observations made at the three stations. The shaded cells
 779 indicate the windflow model that produced the lowest error values for each station. Note that the
 780 depth errors were calculated from mean daily automated measurements while the SWE errors
 781 were the average error values computed on manual observations at near each station during 13
 782 repeated snow surveys.

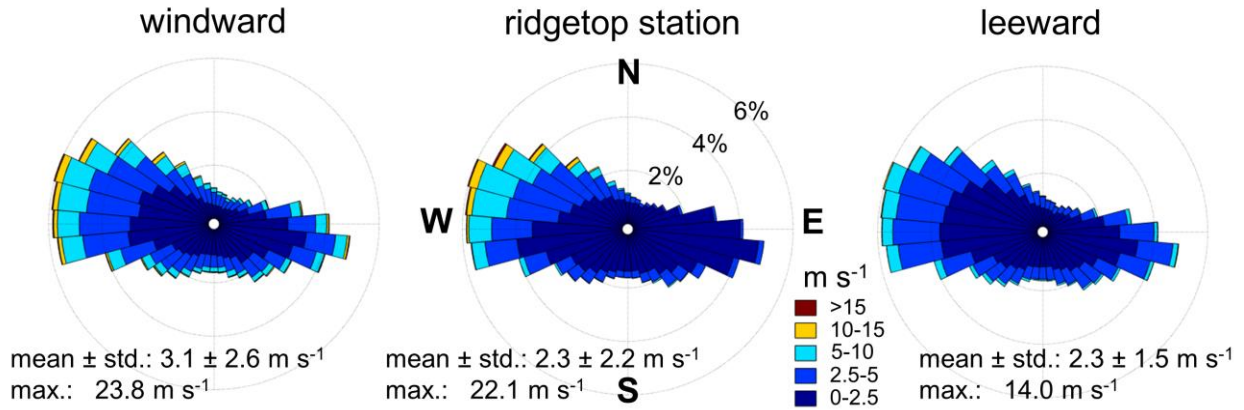
		RMSE			bias		
		windward	ridgetop	leeward	windward	ridgetop	leeward
Depth, cm	LS	22.1	83.4	53.7	16.6	73.9	-38.9
	MS	14.4	9.3	38.1	7.5	3.5	-22.7
	WS	29.3	25.7	27.0	21.4	20.9	-10.0
SWE, mm	LS	91	429	270	70	419	-259
	MS	57	38	170	37	11	-157
	WS	131	110	84	97	101	-66

783



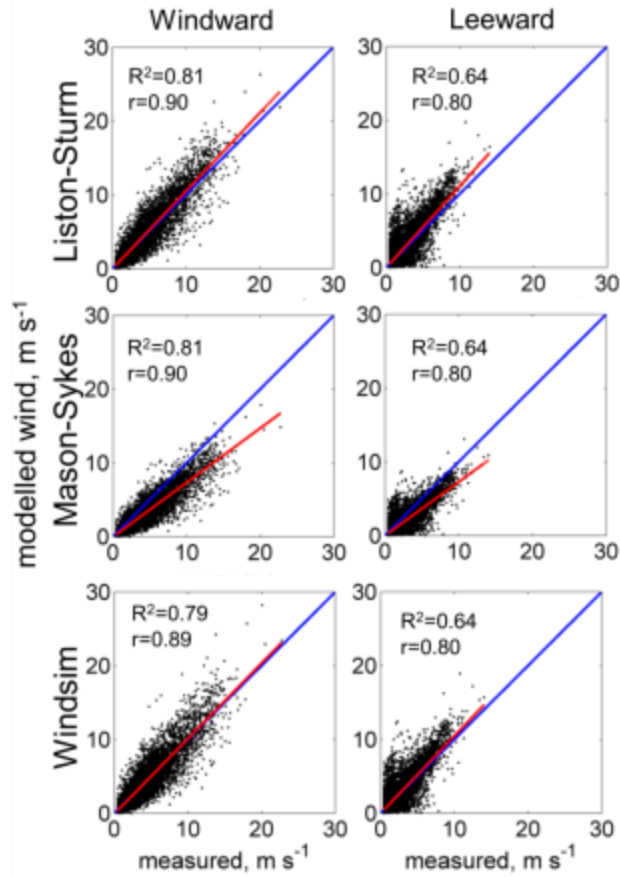
784

785 Figure 1: Study site map showing the nested model domains (24 km x 24 km with 150 m
 786 elevation contour lines; 1.024 km x 1.024 km with 10 m elevation contour lines) centred on the
 787 locations of three meteorological stations on the alpine Fisera Ridge in the Marmot Creek
 788 Research Basin, Alberta, Canada (location indicated by the star in the upper-right panel). The
 789 small maps at right (20 m elevation contour lines) indicate the (top): LiDAR-derived roughness
 790 length values over the inner domain and (bottom): the locations of the snow survey transects
 791 relative to the three meteorological stations. Rectangular domains used to compare spatially
 792 averaged simulated fluxes representative of the windward, ridgetop, and leeward parts of Fisera
 793 Ridge are shown.



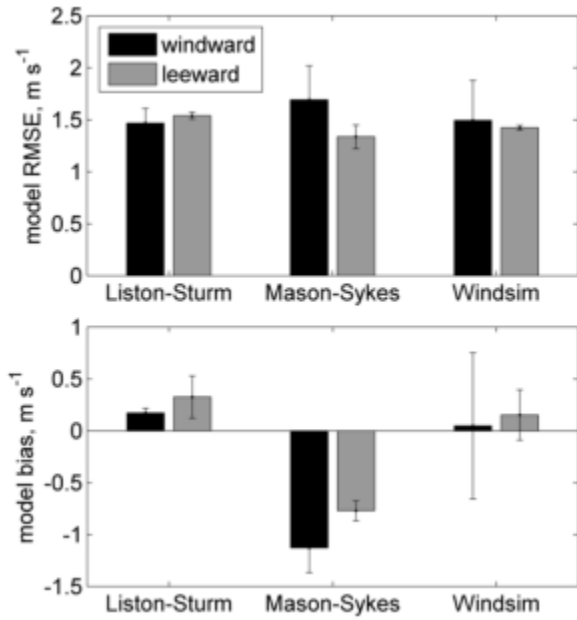
794

795 Figure 2: Wind roses including the mean and maxima wind speeds for the windward, ridgetop
 796 and leeward stations from 15-minute averaged data collected from October, 2008 to September,
 797 2010 (n=57,441). Analysis was limited to time-steps when data were available from all three
 798 stations. Note that wind direction was only measured at the ridgetop station and was assumed
 799 representative of the two other stations for the purposes of the wind rose comparison.



800

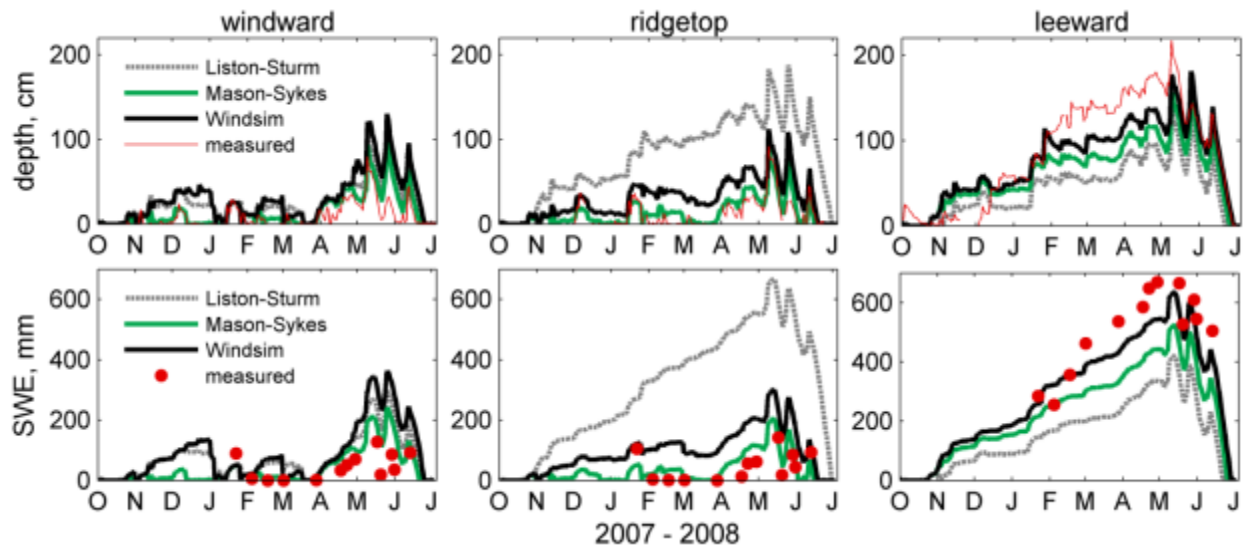
801 Figure 3: Scatter plots of wind speed comparing modelled values (y-axes) from each of the three
 802 windflow models (panel rows) to measured values (x-axes) at the windward (left panels) and
 803 leeward (right panels) automated weather stations. The (linear) regression fits, coefficients of
 804 determination (R^2), and correlation coefficients (r) are indicated.



805

806 Figure 4: Mean (bars) and standard deviation (lines) of modelled wind speed RMSE (top) and
 807 bias (bottom) for the three windflow models compared to measurements at the windward and
 808 leeward automated weather stations.

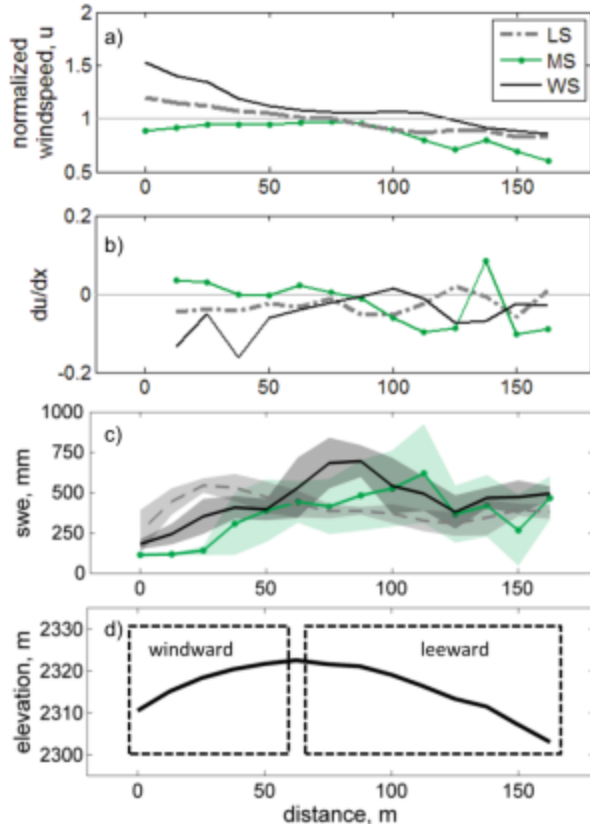
809



810

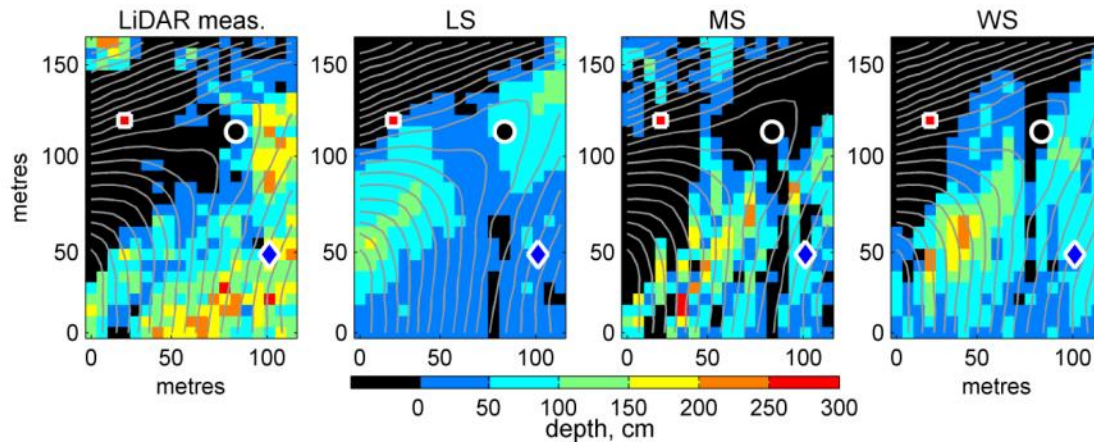
811 Figure 5: Measured snow depth (top) and SWE (bottom) compared to simulated values from the
 812 three windflow models (lines) at the windward (left panel column), ridgetop (centre panel
 813 column), and leeward (right panel column) stations.

814



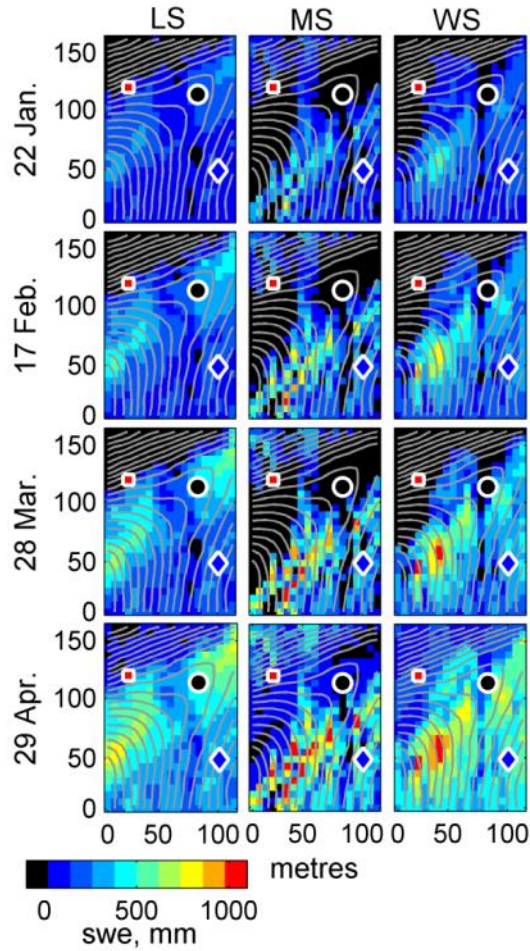
815

816 Figure 6: Modelled a) seasonal mean wind speed normalized by the ridgetop station
817 observations, b) the change in mean wind speed with distance (du/dx), and c) snow water
818 equivalent (SWE) presented as the pixel-wise nearest-neighbor mean (lines) and standard
819 deviation (shading) near the time of seasonal maximum accumulation (May 1, 2008) along d) a
820 160 m linear (12 m vertical) transect from the windward to leeward sides of the alpine ridge.



821

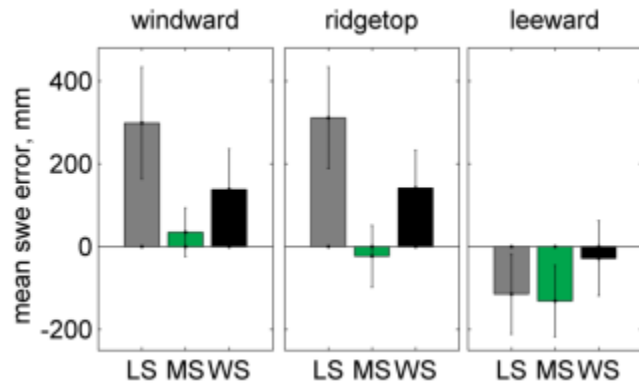
822 Figure 7: The LiDAR-measured snow depth on Fisera Ridge on 28 March, 2008 (left) compared
 823 to that simulated by DSM forced by wind speed output from the Liston-Sturm (LS), Mason-
 824 Sykes (MS) and Windsim (WS) windflow models. The location of the windward (red marker),
 825 ridgetop (black marker), and leeward (blue marker) stations are indicated. The elevation contour
 826 lines are included.



827

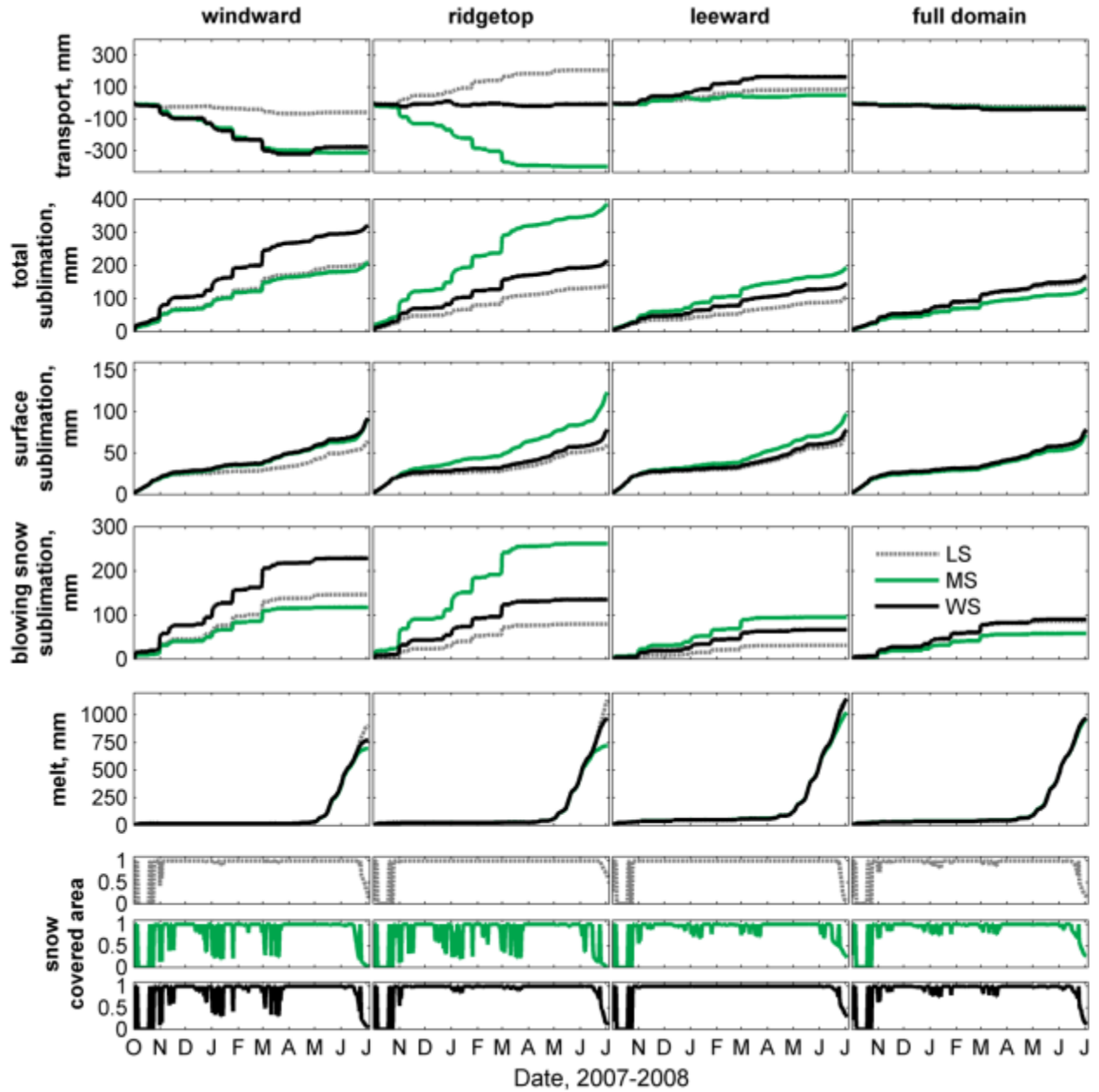
828 Figure 8: Distributed maps of SWE (color scale) near the Fisera Ridge stations (markers) on the
 829 dates of select snow surveys (panel rows) as simulated by DSM forced with output from the
 830 three windflow models (panel columns). Elevation contour lines are included.

831



832

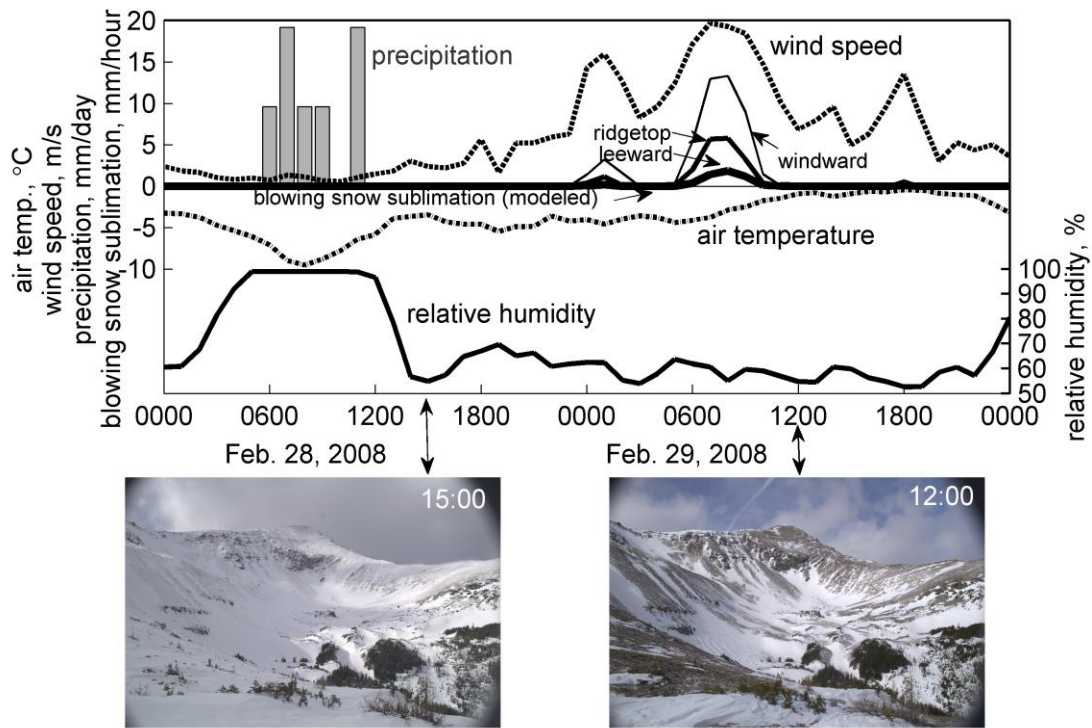
833 Figure 9: Model SWE error computed as the mean (bars) and standard deviation (lines) of
 834 'modelled - measured' SWE averaged along the snow survey transects for 13 surveys on the
 835 windward (left), ridgetop (centre), and leeward (right) sides of Fisera Ridge for the DSM model
 836 forced by wind speed output from the Liston-Sturm (LS), Mason-Sykes (MS) and Windsim
 837 (WS) windflow models.



838

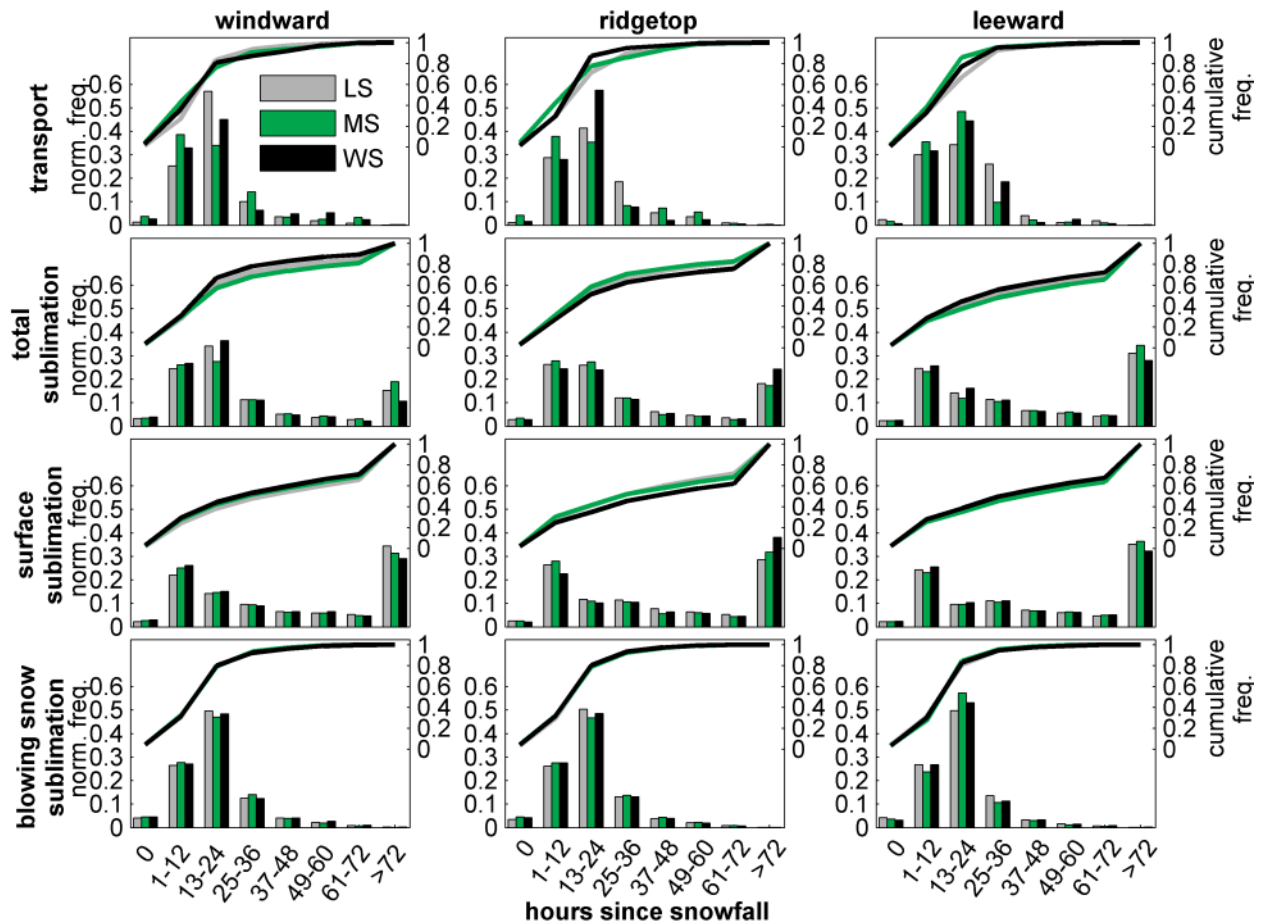
839 Figure 10: Cumulative fluxes of snow transport, sublimation (total, surface and blowing snow
 840 losses), melt, and snow covered area averaged within domains centered on the windward,
 841 ridgetop, leeward, and the entire domain as simulated by DSM forced with wind speed output
 842 from the Liston-Sturm (LS), Mason-Sykes (MS) and Windsim (WS) windflow models for the
 843 2007-2008 snow season.

844



845

846 Figure 11: Measured values of wind speed, air temperature, precipitation (left axis) and relative
 847 humidity (right axis) during a blowing snow event on February 29, 2008 at the Fisera Ridge
 848 (ridgetop) station. Blowing snow sublimation rates estimated by DSM forced with windflow
 849 output from the Windsim model at the locations of the windward, ridgetop and leeward
 850 stations are included. Photographs from a field camera mounted on the ridgetop station looking northwest
 851 toward the windward slope show snow cover before (15:00 Feb. 28) and after (12:00 Feb. 29) the
 852 blowing snow event.



853

854 Figure 12: The timing of normalized (left y-axes) and cumulative (right y-axes) hourly seasonal
 855 snow transport and sublimation (total, surface and blowing snow) fluxes, binned in 12-hour
 856 intervals since the last snowfall (x-axes), as simulated by DSM forced by wind speed output
 857 from the Liston-Sturm (LS), Mason-Sykes (MS) and Windsim (WS) windflow models for the
 858 2007-2008 snow season.

859